Elastic Anisotropy Reversal During Brittle Creep in Shale

Zhi Geng, Audrey Bonnelye, Mian Chen, Yan Jin, Pierre Dick, Christian David, Xin Fang, Alexandre Schubnel

AGU PUBLICATIONS

Geophysical Research Letters

RESEARCH LETTER
10.1002/2017GL074555

Key Points:
- Creep failure strength is ~64% higher than the short-term strength, indicating large strengthening in fault cores during creep deformation
- Reversal of elastic wave anisotropy was observed during creep deformation under upper crustal reservoir conditions
- Microscopic observations revealed crack rotation and pressure solution, implying anisotropy reversal and strength recovery

Supporting Information:
- Supporting Information S1
- Data Set S1

Correspondence to:
Z. Geng,
zhi.geng@ens.fr

Citation:
Geng, Z., Bonnelye, A., Chen, M., Jin, Y., Dick, P., David, C., … Schubnel, A. (2017). Elastic anisotropy reversal during brittle creep in shale. *Geophysical Research Letters*, *44*, 10,887–10,895. https://doi.org/10.1002/2017GL074555

Received 12 JUN 2017
Accepted 14 OCT 2017
Accepted article online 20 OCT 2017
Published online 4 NOV 2017

Elastic Anisotropy Reversal During Brittle Creep in Shale

Zhi Geng[1,2], Audrey Bonnelye[3], Mian Chen[1], Yan Jin[1], Pierre Dick[4], Christian David[5], Xin Fang[1], and Alexandre Schubnel[2]

[1]State Key Laboratory of Petroleum Resources and Engineering, China University of Petroleum, Beijing, China, [2]Laboratoire de Géologie de l'ENS (UMR 8538), PSL Research University, Paris, France, [3]LMS, Ecole Polytechnique, CNRS, Université Paris-Saclay, Palaiseau, France, [4]Institut de Radioprotection et de Sûreté Nucléaire, Fontenay-aux-Roses, France, [5]Département Géosciences & Environnement, Université de Cergy Pontoise, Cergy-Pontoise, France

Abstract We conducted two brittle creep experiments on shale samples under upper crustal conditions (confining pressure of 80 MPa at 26°C and 75°C). We deformed the samples to failure, with bedding oriented perpendicular to the maximum compressive stress direction, using the stress-stepping methodology. In both experiments, the failure stress was ~64% higher than the short-term peak strength. Throughout each differential stress step, ultrasonic wave velocities initially decreased and then gradually increased with deformation/time. The magnitude of these variations depends both on the direction of measurement with respect to the bedding and the temperature, and it is largest for velocities measured parallel to the bedding and at high temperature. Elastic wave anisotropy was completely reversed at 75°C, following a limited amount of axial strain (~0.6%). Scanning electron microscope investigation confirmed evidence of a time-dependent pressure solution, localized compaction, crack sealing/healing, and mineral rotation. Our observations reveal that elastic anisotropy can evolve rapidly in both time and space, which has implications on the stress state and its rotation near fault zones.

1. Introduction

Elastic wave velocities are sensitive to elastic anisotropy in rocks (Guéguen & Palciauskas, 1994; Mavko et al., 2009; O'Connell & Budiansky, 1974; Sayers & Kachanov, 1995). Intrinsic or matrix anisotropy exhibits little pressure dependence and is generally induced by a fabric of mineral phases, that is, crystallographic- or shape-preferred orientations. Extrinsic anisotropy is sensitive to both pressure and differential stress (e.g., Sayers & Kachanov, 1995; Schubnel et al., 2005) and is generated by oriented crack networks. The interplay between extrinsic and intrinsic elastic anisotropies with stress, pressure, strain, and time in the deforming rock material is a complex problem that has largely been disregarded until now. Indeed, most experimental studies have concentrated either on the evolution of anisotropy with pressure in initially anisotropic rocks (e.g., Kern, 1993; Kern et al., 2008; Nishizawa & Kanagawa, 2010) or on the development of anisotropy of initially isotropic material under differential stress (e.g., Schubnel & Guéguen, 2003; Wang et al., 2012, 2013). Brantut (2015) recently demonstrated that elastic anisotropy was time, stress, and pressure dependent.

In the upper crust, deformation is dominated by brittle fractures along faults, so that the elastic anisotropy of rocks in areas with low background matrix anisotropy is mainly due to cracks (Guéguen & Sarout, 2009). At the kilometer scale, elastic wave anisotropy has, thus, become a primary observable variable to explore the geometry of faults and the state of the underground stress. For instance, Mizuno et al. (2005) used shear wave splitting recordings of microearthquakes to investigate the stress rotation on the Atotsugawa fault. Boness and Zoback (2006) reviewed the mechanisms of shear wave splitting and classified them into two major categories: stress-induced anisotropy and structural anisotropy. However, shales and clay material have been found ubiquitously within faults and fault gouges (Solum et al., 2006), and shales are known to exhibit both intrinsic and extrinsic anisotropies. In addition, during the deformation of shales, fracturing processes interact with pressure solution creep (Gratier et al., 2013), a fundamental mechanism at play during the mechano-chemical compaction of sediments in the upper crust (2–10 km) that makes it behave in both a brittle and viscous manner (Gratier et al., 1999). These two mechanisms operate on two different timescales: brittle deformation for short times and pressure solution for long times.

Recently, Bonnelye et al. (2017a, 2017b) studied the influence of bedding and stress on elastic wave anisotropy in "anisotropic" Tournemire shale samples deformed at constant strain rates. To our knowledge, only

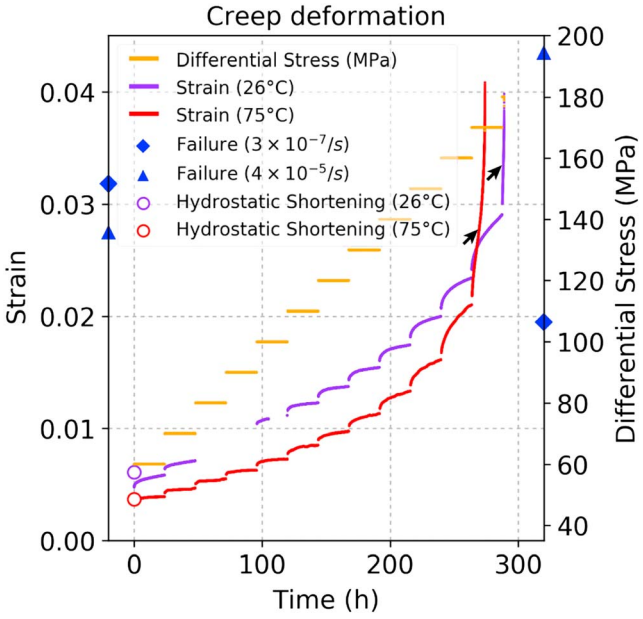

Figure 1. Differential stress (yellow) and corresponding axial deformation (purple and red lines) as a function of time, at 26°C and 75°C. The diamond and triangle symbols represent the peak strength and failure strain of two reference samples, which were deformed in conventional triaxial experiments conducted by Bonnelye et al. (2017b) under a constant strain rate of 3×10^{-7}/s and 4×10^{-5}/s, respectively. The black arrows indicate the moment of strain acceleration (tertiary creep) leading to failure. The gaps in the strain curve (26°C) resulted from technical issues with the recording system.

a few studies (Li & Ghassemi, 2012; Sone & Zoback, 2014; Zhao & Roegiers, 1995) have been carried out on the brittle creep behavior of shale until now. Indeed, most studies on brittle creep have focused on igneous rocks (Fujii et al., 1999; Heap et al., 2011; Kranz, 1980; Ross et al., 1983) and porous sedimentary rocks (Brantut et al., 2013; Cogan, 1976; Heap et al., 2009; Hettema et al., 1991; Ngwenya et al., 2001). We study here the evolution of elastic wave anisotropy during the brittle creep deformation of Tournemire shale.

2. Materials and Methods

Samples were sourced from the underground laboratory of the French Institut de Radioprotection et Sûreté Nucléaire in Tournemire (southern France). The tunnel is located in a shaly Toarcian layer. A general description of the structure and mechanical/physical properties of Tournemire argillaceous media are provided in Cabrera et al. (2001) and Valès et al. (2004). For this study, two cores, each with a diameter of 42 mm, were prepared with the long axis perpendicular to the natural bedding. Coring was done using air as a cooling fluid, and the fracture regions were avoided. Following coring, the cores were immediately placed in vacuum-sealed bags to avoid dehydration. The natural water content of the samples is approximately 5% (Bonin, 1998; Schmitt, 1994). Immediately prior to testing, the samples were dry-polished at both ends to a total length of 84.5 (±0.1) mm, to ensure that both ends were planar and parallel.

The triaxial apparatus used in this study is an externally heated oil-medium confining cell installed at the Laboratoire de Géologie of ENS-Paris (France). A detailed description and a schematic view of this apparatus can be found in Brantut et al. (2011). Three external capacitive gap sensors were used to measure axial shortening during deformation. The averaged displacement of these sensors, corrected for machine stiffness, was used to calculate the axial strain. Given the extremely low permeability of shales, our laboratory experiments were done without controlling for pore pressure. The pore pressure system was vented to an ambient environment. Two samples with initial saturation were loaded separately, one at room temperature (26°C, referred hereafter as sample RT) and the other one at high temperature (75°C, referred hereafter as sample HT). Samples were first hydrostatically loaded to 80 MPa at a rate of 0.3 MPa/min. Then sample HT was heated to 75°C after pressurization within the confining cell at a rate of 0.5°C/min. Confining pressure and temperature were then maintained constant for ~18 h. Next, differential stress ($\sigma_1 - \sigma_3$) was increased from 0 to 60 MPa at a rate of 0.5 MPa/min and then held constant for 24 h. In the following days, the axial stress was increased by 10 MPa at the same rate and kept constant for 24 h repeatedly, until failure was achieved (see Figure 1). Stress and strain recordings were sampled at 0.5 Hz.

To monitor the evolution of ultrasonic *P* wave anisotropy during the experiments, we glued 16 piezoceramic-based transducers (shown in supporting information Figure S1) directly to the sample. Details on the piezoceramics and configuration of transducers can be found in Brantut et al. (2014a). All 16 transducers were consecutively pulsed with a voltage of 500 V (1 μs rise time), so that each sensor was used once as a source and recorded by the rest of the transducer network during what is referred to as a velocity survey. A stack of 10 signals was performed to enhance the signal-to-noise ratio. Ultrasonic signals were amplified to 45 dB and recorded on a 16-channel digital encoder at 10 MHz sampling frequency. We used these recordings to determine the *P* wave travel times in the sample along selected raypaths. Given the large amount of data to be computed, we applied a cross-correlation method (Pettitt et al., 2002) to automatically pick travel time differences with a reference survey, which was performed after hydrostatic compression. Travel times were then converted into elastic wave velocities. Absolute errors in velocities were estimated to be in the order of a few percent (~2%).

The acoustic ray angle (ϕ in supporting information Figure S1) is defined as the angle between the raypath and the normal to the bedding plane. Assuming that our shale samples are transversely isotropic and homogeneous, we estimated *P* wave velocities at different ray angles (90°, 71°, 55.4°, 44°, and 36°) by averaging *P* wave velocities measured along raypaths with the same ray angle. We only selected raypaths that cross the symmetry axes of the samples. Velocity surveys were performed every 5 min during the period of increasing axial stress and at every 15 or 30 min when the stress was kept constant.

3. Results

3.1. Stress and Strain Curves

Due to thermal expansion and hardening during hydrostatic loading, sample HT (75°C) exhibited less hydrostatic shortening but larger failure strain and faster strain rates (denoted by the gradient of the curve), approaching failure (see Figure 1). Sample HT (75°C) failed at a differential stress of 170 (±0.1) MPa and reached an axial strain of 0.0408 ($\pm 10^{-4}$) at failure. Sample RT (26°C) failed at a differential stress of 180 (±0.1) MPa after an axial strain of 0.0396 ($\pm 10^{-4}$).

For comparison, Bonnelye et al. (2017b) conducted two conventional (constant strain rate) triaxial experiments at room temperature (26°C) using the same material under the same orientation and a confining pressure of 80 MPa. In those experiments, the peak strength and failure strain of samples were 106 MPa and 0.0318, respectively, under a constant strain rate of 3×10^{-7}/s, and 194 MPa and 0.0275, respectively, under a constant strain rate of 4×10^{-5}/s (see the diamond and triangle symbols in Figure 1). Our creep samples exhibited strengths (170/180 MPa) similar to the samples of Bonnelye et al. (2017b) that were deformed at a fast constant strain rate (4×10^{-5}/s) but a ~64% higher strength than those deformed at the strain rate of 3×10^{-7}/s. Note that the constant strain rate of those reference experiments was about 2 to 3 orders of magnitude higher than the creep strain rates (~10^{-9}/s) estimated in our experiments, except during the last stage (strain rate $\geq 10^{-6}$/s) during which the samples accelerated to failure.

3.2. Temporal Variation of Ultrasonic *P* Wave Velocities

At both temperatures (26°C and 75°C), *P* wave velocities at various ray angles tended to converge during the early stage of loading (strains of 0–0.005 in Figures 2a and 2b), indicating a decrease in the apparent *P* wave anisotropy. Overall, velocities increased in the first half of the experiments and then decreased dramatically when approaching failure. The magnitudes of decrease and increase were highly dependent on both the raypath and temperature. At 26°C, the original fast *P* wave direction at a ray angle of 90° became the direction of the slow *P* wave after an axial strain of 0.035, that is, when the sample accelerated to creep failure during the final constant stress step. For comparison, at 75°C, both the fast and slow *P* wave completely reversed after an axial strain of only 0.006.

A closer analysis shows that the ultrasonic *P* wave velocities, regardless of the ray angle, also decreased and then increased gradually during each creep step (insets in Figures 2a and 2b). Again, the magnitude of increase was dependent on the ray angles and was larger at high temperature than at room temperature. For instance, within the strain range of 0.005–0.015, the *P* wave velocity measured parallel to the bedding (90°) decreased first and then increased gradually, while the velocity at ray angle 36° kept increasing. We observed a gradual transition from high ray angles to low ray angles, the former displaying a more apparent decreasing trends while the latter showing greater increasing trends.

4. Discussion

4.1. Strength Recovery Mechanisms During Creep Deformation

A general understanding of rock strength states that the failure strength of rock deformed at a lower strain rate is smaller than the peak strength induced under a higher deformation rate (Bhat et al., 2012; Bonnelye et al., 2017b; Brantut et al., 2013; Peng & Podnieks, 1972). A possible explanation for the strength recovery of our nearly 10 day experiments is the occurrence of creep compaction (Brantut et al., 2014b), pressure solution creep (Gratier et al., 2013, 1999), and crack sealing (Renard et al., 2000) during deformation. Such time-dependent strengthening, originating from crack sealing, has been observed in several studies (Brantut et al., 2014b; Gratier et al., 2013, 1999; Hickman & Evans, 1992; Meredith, 2013; Renard et al., 2000; Tenthorey et al., 2003).

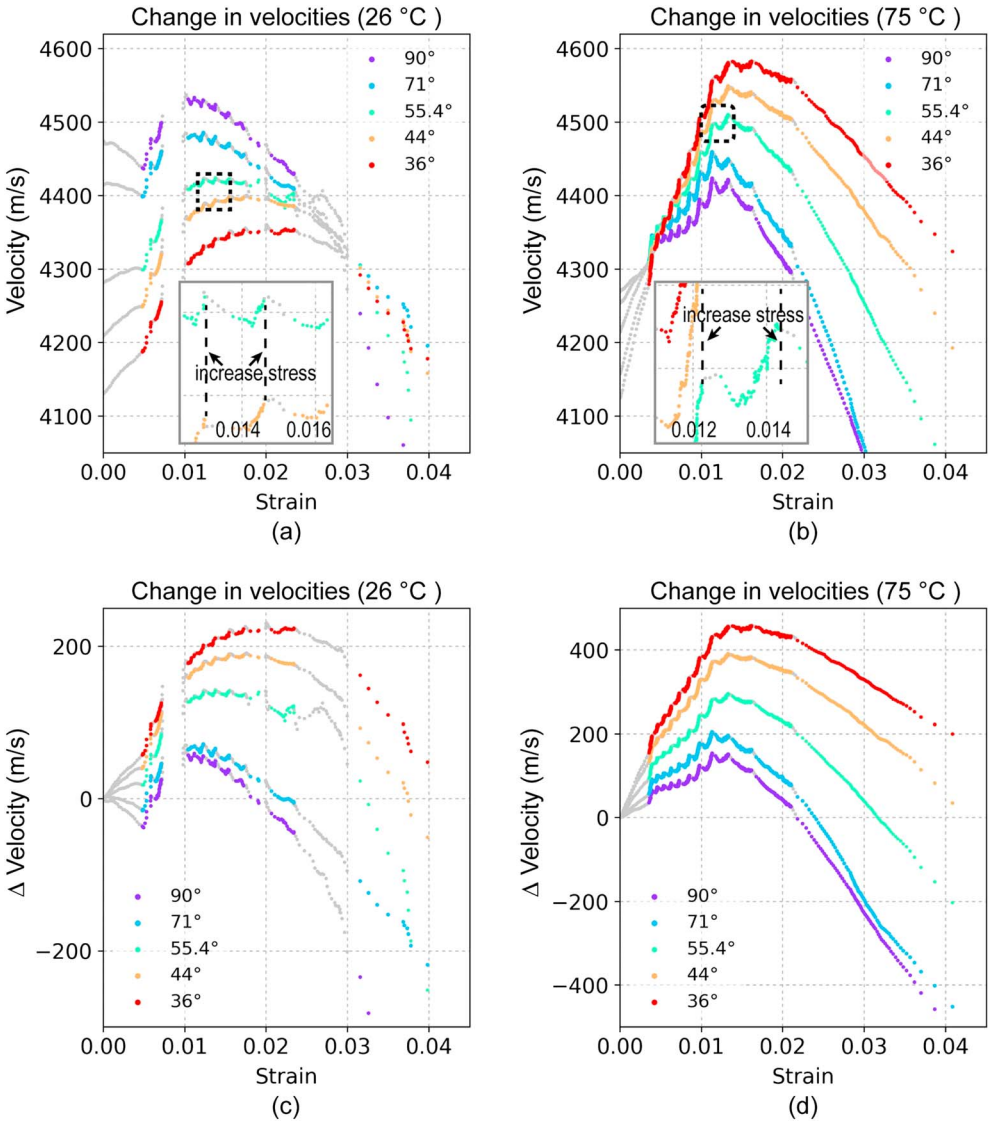

Figure 2. *P* wave velocities of samples deformed at (a) 26°C and (b) 75°C as a function of strain. *P* wave velocity differences are presented with respect to the measurements at hydrostatic conditions (80 MPa) at (c) 26°C and (d) 75°C. The gray dots represent measured velocities during the period of increasing differential stress; the colored dots represent measured velocities under constant differential stress.

The velocity difference is a good indicator of internal microstructural changes to the samples. Figures 2c and 2d display differences in *P* wave velocities relative to the reference value measured under hydrostatic conditions. The relative velocity difference at a low ray angle is larger than that at a high ray angle. The variation range within a specific creep period is wider (nearly double) at 75°C. The changes in V_p gradually reduced after nearly 8 h (one third elapsed time) of creep, after which V_p remained almost constant under negligible strain accumulation. A possible interpretation is that during each axial stress step, stress-induced subvertical cracks were initiated and propagated then gradually closed and sealed during creep deformation. The increasing axial stress gradually squeezed the interspace between the beddings. Accordingly, grain contacts were reinforced, and the new deformation features gradually overprinted the initial anisotropy pattern. This overprinting seemed to be more effective at the higher temperature. Again, one should stress that a complete reversal was attained for only a limited amount of axial strain and cannot be explained solely by crack growth.

Taken together, our ultrasonic *P* wave data suggest competition between crack growth, sealing/healing, and possible pressure solution, mineral rotation, or anisotropic compaction during creep. If creep deformation

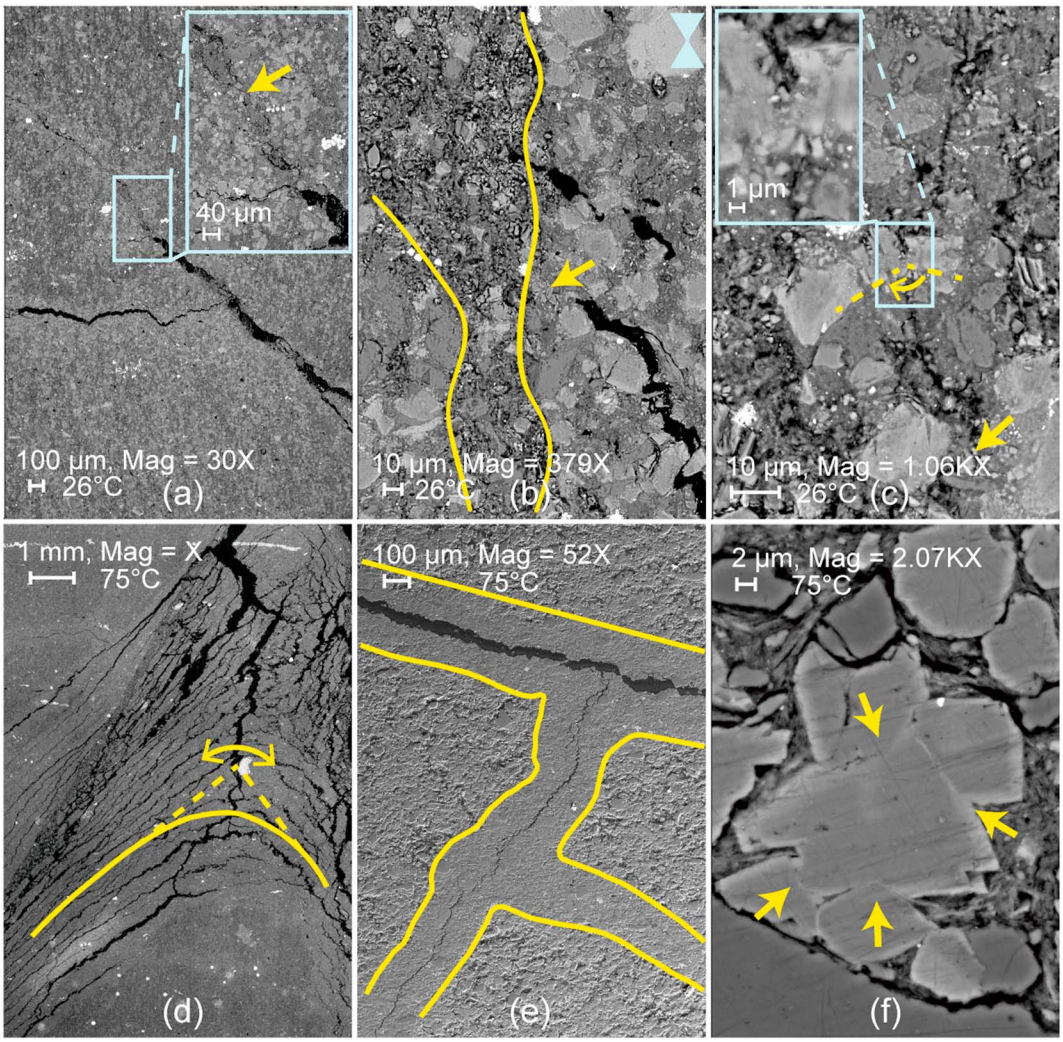

Figure 3. Scanning electron microscope (SEM) images in the failure zone. Sample RT (26°C): (a) shear area with visible cracks, (b) deformed/damage region with microcracks, and (c) rock matrix near failure plane. Sample HT (75°C): (d) macroscopic shear zone, (e) consolidation/compaction bands, and (f) evidence of pressure solution of dolomite grains within a compaction band. In all the figures, the direction of axial stress is vertical, while the natural beddings are horizontal. Figures 3a–3d and 3f are backscattered electrons (BSE) images, and Figure 3e is a secondary electrons (SE) image.

was partially driven by pressure solution, which is stress, time, and temperature dependent, one should expect that the longer the stress step and the higher the temperature or differential stress, the greater the consolidation should occur. Indeed, higher consolidation is observed with increasing temperature and differential stress. For the latter, this is only true until a critical differential stress is attained, beyond which brittle processes (fracture propagation) that lead to failure begin to dominate creep deformation.

Microstructural observations shed light on both strength recovery and time-dependent acoustic anisotropy. Scanning electron microscope (SEM) images were taken in the vicinity of the failure plane of the two samples (Figure 3). Evidence for sealing or filling in fractures was ubiquitous (Figures 3a–3c). A vertical microcrack sealed within a calcite grain (Figure 3c) is a potential indicator that the pressure solution was active during the deformation of our samples, even at 26°C. The grain was clearly broken and had undergone rotation during its deformation history. The postmortem microstructure of sample HT (75°C) reveals a clear rotation of microcracks (Figure 3d), a feature that may be coincident with the observed anisotropy reversal of *P* wave velocities. Bonnelye et al. (2017a) also observed, under similar conditions but at a higher magnification, clear evidence of clay mineral platelet rotation in the vicinity of the macroscopic shear fracture. Figure 3e displays

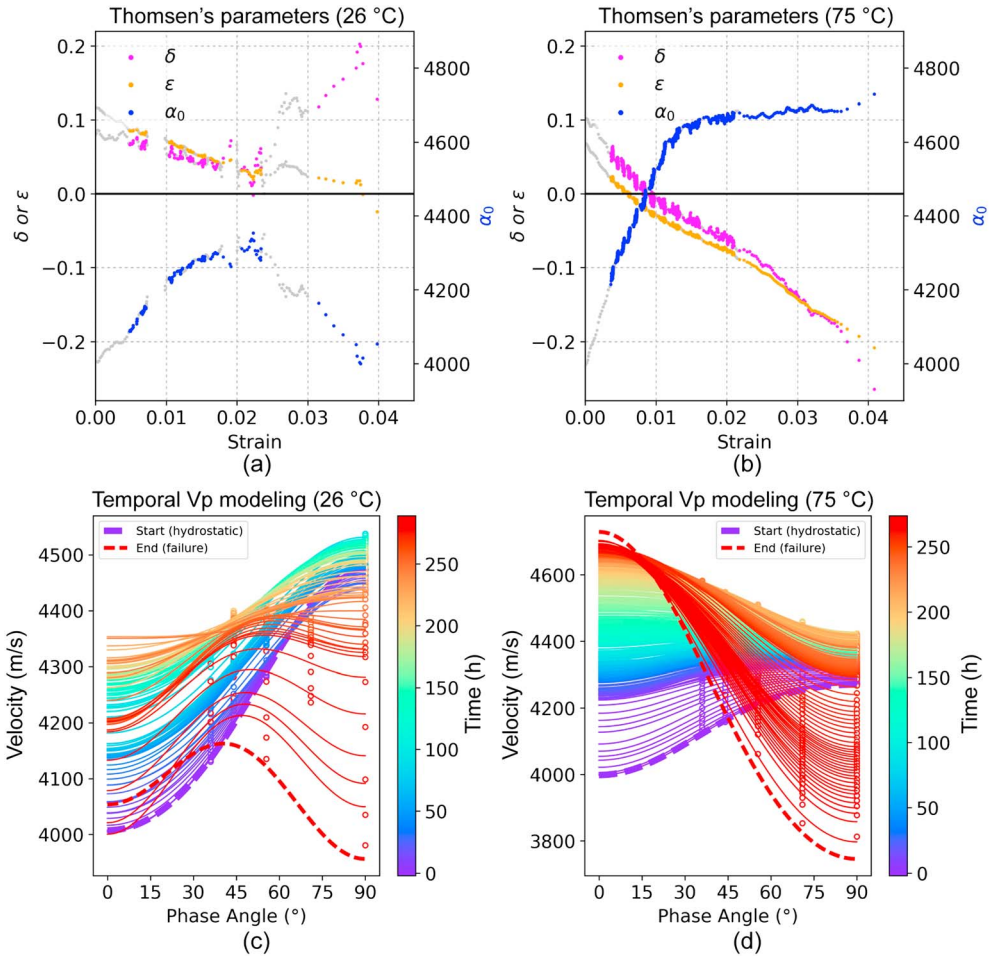

Figure 4. Evolution of *P* wave anisotropy (Thomsen's parameters α_0, δ, and ε) as a function of strain at (a) 26°C and (b) 75°C. Evolution of modeled *P* wave velocities using Thomsen's parameters in time series as a function of phase (ray) angle at (c) 26°C and (d) 75°C. The open circles denote experimental measurements, and the colored bar represents time relative to the start of the first stress step.

evidence that localized creep compaction was active during deformation, with the formation of low porosity consolidation bands along fractures. Within these bands, dolomite grains exhibit evidence of pressure solution (Figure 3f). This observation confirms the conclusion of Zhang et al. (2010), who suggested that creep compaction in wet granular calcite occurred owing to the diffusion-controlled intergranular pressure solution at low strain, giving way to precipitation control at larger strains over practicable laboratory timescales. Here we observe that the pressure solution is indeed thermally activated, as little evidence of the solution was found in sample RT (26°C), and larger strains/velocity increases were observed in sample HT (75°C). Note that it is likely that clay particles enhance pressure solution creep because they allow faster diffusion of solutes from the particle contacts to the pore space and inhibit grain boundary formation (Renard et al., 2001). Finally, one should keep in mind that these images are postmortem observations, and it seems likely that the fractures observed within localized compaction bands are decompressive features.

4.2. *P* Wave Anisotropy Reversal

As our samples are weakly anisotropic ($-0.2 < \varepsilon < 0.2$), we inverted *P* wave velocities into three independent Thomsen's parameters (α_0, δ, and ε) (Thomsen, 1986) using a least squares fit method (Bonnelye et al., 2017a) (see Figures 4a and 4b). The parameter α_0 is the *P* wave velocity measured along the transverse isotropy symmetry axis (vertical and perpendicular to the bedding). The parameter δ characterizes the anellipticity of the *P*

wave field, and ε is a direct measure of *P* wave anisotropy between the transverse isotropy axis of symmetry (0°) and along the bedding (90°). Parameter α_0 increased systematically during the early stage of experiments, from ~4,000 m/s to ~4,300 m/s at 26°C and to ~4,700 m/s at 75°C. As expected, the magnitude of the increase in α_0 is paramount during the creep stages at high temperature. At room temperature, α_0 exhibited a continuous decrease beyond an axial strain of ~0.022 to its initial value, ~4,000 m/s, at failure. For comparison, at 75°C, α_0 remained constant up to failure, which highlights that the velocity perpendicular to the bedding is not affected by macroscopic failure.

At 26°C, δ and ε linearly decreased with increasing strain during the early part of the experiment (Figure 4a). Close to failure, the evolution of δ and ε diverged, and ε became negative, meaning that the anisotropy reversed. At failure, $\varepsilon \sim -0.03$, indicating that the *P* wave anisotropy reversed and reached approximately 3% in the opposite orientation. In other words, the *P* wave propagating along the bedding (90°), which was originally the fastest, became the slowest wave. At 75°C, the *P* wave anisotropy completely reversed, so ε became negative after the third stress step (80 MPa of differential stress), after an axial strain of only ~0.006. At failure, $\varepsilon \sim -0.2$; thus, the final anisotropy not only reversed but was also twice as strong as the initial value. It is interesting to note that both δ and ε continuously decreased linearly with increasing strain, even during the last stages of this experiment.

We then used the inverted parameters to calculate the theoretical values of velocities as a function of the ray angle (Figures 4c and 4d). Under hydrostatic conditions, the fast *P* wave velocity was the one propagating along the bedding (90°). At 26°C, the fast *P* wave slowly rotated toward the slower propagation direction and near the end of the experiment; the fastest *P* wave was the one propagating along the direction of maximum shear, at 45° (Figure 4c). Note that in this case, the wavefront is extremely anelliptical. In contrast, at 75°C, the direction of the fast *P* wave completely switched from 90° (along bedding) to 0° (vertical) and vice versa (from 0° to 90°) for the slow *P* wave, after an axial strain of only ~0.006 and ~70 h of deformation (Figure 4d). In this case, one can clearly see that the magnitude of anisotropy is greater at the end of the experiment than initially. Again, such an increase in the *P* wave velocity perpendicular to the bedding is difficult to explain solely by the closure of microcracks, since the final velocity is much larger than the velocity initially measured along the bedding under pressure.

5. Conclusions and Implications

Our microstructural observations revealed that *P* wave anisotropy reversal results from a multitude of factors including stress-induced rotation of microcrack orientation, preferred orientation of dominant grains, temperature, and time-dependent pressure solution, and sealing or healing of microcracks. The time-dependent rotation of the fast *P* wave direction highlights the complex contemporaneous evolution of intrinsic (mineral fabric-related) and extrinsic (crack-related) anisotropy within relatively short time periods and for unexpectedly small strain values in semibrittle materials. Elastic wave anisotropy reversal potentially provides an appealing additional explanation for local stress rotation observed near active faults (Faulkner et al., 2006; Healy, 2008).

Our laboratory results also indicate that during deformation experiments of Tournemire shale, localized compaction, pressure solution, sealing, and healing of cracks contributed not only to recovery of elastic wave speeds but also to strengthening. In light of these results, one may wonder whether our samples would have failed at low differential stress or whether they would have simply hardened by compaction (Brantut et al., 2014b). In the latter case, this would have important implications for the strength of accretionary prisms and shallow fault zones, often constituted of clay materials (Chester et al., 2013; Hirono et al., 2014; Solum et al., 2006; Yamaguchi et al., 2011). The short-term brittle strength measurements of shaly fault cores may, in fact, have few physical implications on the long-term (weeks to millions of years) mechanical strength of these materials at the field scale, as reasoned by Gratier et al. (2013).

Elastic wave anisotropy and, in particular, shear wave splitting, the easiest anisotropic feature to be measured at the field scale, have become a primary tool for imaging the stress field (Boness & Zoback, 2006; Crampin & Lovell, 1991; Mizuno et al., 2005). Although we measured only *P* wave velocities, our data also provide important constraints on shear wave splitting. Indeed, within a transversely isotropic medium, if the sample exhibits radial *P* wave anisotropy, it will exhibit azimuthal *S* wave anisotropy as well (see Mavko et al., 2009; Schubnel &

Guéguen, 2003). Accordingly, shear wave anisotropy (or splitting) is likely to exhibit time series variation similar to that of V_p anisotropy, shown in Figures 4c and 4d. We can therefore suspect that shear wave splitting may also rotate quite rapidly, both in time and space. This may be particularly true in the vicinity of fault zones and is important to keep in mind while interpreting the shear wave splitting pattern at the field scale.

Finally, the anisotropy reversal of ultrasonic *P* wave velocities was observed for limited amounts of strain and time in our study. Thus, it is possible that part of the postseismic relaxation observed along fault zones at shallow depths using noise tomography over monthly timescales (Brenguier et al., 2008) may also correspond to changes in anisotropy and stress variations/rotations. On the other hand, the direction of the fast *P* wave and the magnitude of anisotropy continuously evolved during creep deformation, which might be imaged at the field scale using shear wave splitting or noise tomography near fault zones.

Acknowledgments
This research was founded by the National Natural Science Foundation of China (Major Program 51490651). We thank Damien Deldicque and Yves Pinquier (ENS-Paris) for their technical support, the Associate Editor, an anonymous reviewer, Marie Violay, and Harsha Bhat for their insightful suggestions, which helped improve the quality of this manuscript. The data produced during our experiments are available in the supporting information.

References

Bhat, H. S., Rosakis, A. J., & Sammis, C. G. (2012). A micromechanics based constitutive model for brittle failure at high strain rates. *Journal of Applied Mechanics*, *79*(3), 031016. https://doi.org/10.1115/1.4005897

Boness, N. L., & Zoback, M. D. (2006). Mapping stress and structurally controlled crustal shear velocity anisotropy in California. *Geology*, *34*(10), 825–828. https://doi.org/10.1130/G22309.1

Bonin, B. (1998). Deep geological disposal in argillaceous formations: Studies at the Tournemire test site. *Journal of Contaminant Hydrology*, *35*(1–3), 315–330. https://doi.org/10.1016/S0169-7722(98)00132-6

Bonnelye, A., Schubnel, A., David, C., Henry, P., Guglielmi, Y., Gout, C., … Dick, P. (2017a). Elastic wave velocity evolution of shales deformed under uppermost crustal conditions. *Journal of Geophysical Research: Solid Earth*, *122*, 130–141. https://doi.org/10.1002/2016JB013540

Bonnelye, A., Schubnel, A., David, C., Henry, P., Guglielmi, Y., Gout, C., … Dick, P. (2017b). Strength anisotropy of shales deformed under uppermost crustal conditions. *Journal of Geophysical Research: Solid Earth*, *122*, 110–129. https://doi.org/10.1002/2016JB013040

Brantut, N. (2015). Time-dependent recovery of microcrack damage and seismic wave speeds in deformed limestone. *Journal of Geophysical Research: Solid Earth*, *120*, 8088–8109. https://doi.org/10.1002/2015JB012324

Brantut, N., Heap, M. J., Baud, P., & Meredith, P. G. (2014a). Rate-and strain-dependent brittle deformation of rocks. *Journal of Geophysical Research: Solid Earth*, *119*, 1818–1836. https://doi.org/10.1002/2013JB010448

Brantut, N., Heap, M. J., Baud, P., & Meredith, P. G. (2014b). Mechanisms of time-dependent deformation in porous limestone. *Journal of Geophysical Research: Solid Earth*, *119*, 5444–5463. https://doi.org/10.1002/2014JB011186

Brantut, N., Heap, M. J., Meredith, P., & Baud, P. (2013). Time-dependent cracking and brittle creep in crustal rocks: A review. *Journal of Structural Geology*, *52*, 17–43. https://doi.org/10.1016/j.jsg.2013.03.007

Brantut, N., Schubnel, A., & Guéguen, Y. (2011). Damage and rupture dynamics at the brittle-ductile transition: The case of gypsum. *Journal of Geophysical Research*, *116*, B01404. https://doi.org/10.1029/2010JB007675

Brenguier, F., Campillo, M., Hadziioannou, C., Shapiro, N., Nadeau, R. M., & Larose, E. (2008). Postseismic relaxation along the San Andreas fault at Parkfield from continuous seismological observations. *Science*, *321*(5895), 1478–1481. https://doi.org/10.1126/science.1160943

Cabrera, J., Beaucaire, C., Bruno, G., De Windt, L., Genty, A., Ramambasoa, N., … Volant, P. (2001). Projet Tournemire–Synthèse des programmes de recherche 1995–1999, Report IPSN DPRE/SERGD, 01-19.

Chester, F. M., Rowe, C., Ujiie, K., Kirkpatrick, J., Regalla, C., Remitti, F., … Bose, S. (2013). Structure and composition of the plate-boundary slip zone for the 2011 Tohoku-Oki earthquake. *Science*, *342*(6163), 1208–1211. https://doi.org/10.1126/science.1243719

Cogan, J. (1976). Triaxial creep tests of Opohonga limestone and Ophir shale. In *International journal of rock mechanics and mining sciences & geomechanics abstracts* (Vol. 13, pp. 1–10). Pergamon. https://doi.org/10.1016/0148-9062(76)90221-7

Crampin, S., & Lovell, J. H. (1991). A decade of shear-wave splitting in the Earth's crust: What does it mean? What use can we make of it? And what should we do next? *Geophysical Journal International*, *107*(3), 387–407. https://doi.org/10.1111/j.1365-246X.1991.tb01401.x

Faulkner, D., Mitchell, T., Healy, D., & Heap, M. (2006). Slip on'weak'faults by the rotation of regional stress in the fracture damage zone. *Nature*, *444*(7121), 922–925. https://doi.org/10.1038/nature05353

Fujii, Y., Kiyama, T., Ishijima, Y., & Kodama, J. (1999). Circumferential strain behavior during creep tests of brittle rocks. *International Journal of Rock Mechanics and Mining Sciences*, *36*(3), 323–337. https://doi.org/10.1016/S0148-9062(99)00024-8

Gratier, J.-P., Dysthe, D. K., & Renard, F. (2013). The role of pressure solution creep in the ductility of the Earth's upper crust. *Advances in Geophysics*, *54*, 47–179. https://doi.org/10.1016/B978-0-12-380940-7.00002-0

Gratier, J.-P., Renard, F., & Labaume, P. (1999). How pressure solution creep and fracturing processes interact in the upper crust to make it behave in both a brittle and viscous manner. *Journal of Structural Geology*, *21*(8–9), 1189–1197. https://doi.org/10.1016/S0191-8141(99)00035-8

Guéguen, Y., & Palciauskas, V. (1994). *Introduction to the physics of rocks*. Princeton, NJ: Princeton University Press.

Guéguen, Y., & Sarout, J. (2009). Crack-induced anisotropy in crustal rocks: Predicted dry and fluid-saturated Thomsen's parameters. *Physics of the Earth and Planetary Interiors*, *172*(1–2), 116–124. https://doi.org/10.1016/j.pepi.2008.05.020

Healy, D. (2008). Damage patterns, stress rotations and pore fluid pressures in strike-slip fault zones. *Journal of Geophysical Research*, *113*, B12407. https://doi.org/10.1029/2008JB005655

Heap, M., Baud, P., Meredith, P., Bell, A., & Main, I. (2009). Time-dependent brittle creep in Darley dale sandstone. *Journal of Geophysical Research*, *114*, B07203. https://doi.org/10.1029/2008JB006212

Heap, M. J., Baud, P., Meredith, P. G., Vinciguerra, S., Bell, A. F., & Main, I. G. (2011). Brittle creep in basalt and its application to time-dependent volcano deformation. *Earth and Planetary Science Letters*, *307*(1–2), 71–82. https://doi.org/10.1016/j.epsl.2011.04.035

Hettema, M. H. H., De Pater, C. J., & Wolf, K. H. (1991). Effects of temperature and pore water on creep of sandstone rock. In *The 32nd US Symposium on Rock Mechanics (USRMS)*. American Rock Mechanics Association.

Hickman, S. H., & Evans, B. (1992). Growth of grain contacts in halite by solution-transfer: Implications for diagenesis, lithification, and strength recovery. *International Geophysics*, *51*, 253–280.

Hirono, T., Kameda, J., Kanda, H., Tanikawa, W., & Ishikawa, T. (2014). Mineral assemblage anomalies in the slip zone of the 1999 Taiwan chi-chi earthquake: Ultrafine particles preserved only in the latest slip zone. *Geophysical Research Letters*, *41*, 3052–3059. https://doi.org/10.1002/2014GL059805

Kern, H. (1993). *P*-and *S*-wave anisotropy and shear-wave splitting at pressure and temperature in possible mantle rocks and their relation to the rock fabric. *Physics of the Earth and Planetary Interiors*, *78*(3–4), 245–256. https://doi.org/10.1016/0031-9201(93)90159-7

Kern, H., Ivankina, T., Nikitin, A., Lokajíček, T., & Pros, Z. (2008). The effect of oriented microcracks and crystallographic and shape preferred orientation on bulk elastic anisotropy of a foliated biotite gneiss from Outokumpu. *Tectonophysics*, *457*(3–4), 143–149. https://doi.org/10.1016/j.tecto.2008.06.015

Kranz, R. L. (1980). The effects of confining pressure and stress difference on static fatigue of granite. *Journal of Geophysical Research*, *85*(B4), 1854–1866. https://doi.org/10.1029/JB085iB04p01854

Li, Y., & Ghassemi, A. (2012). *Creep behavior of Barnett, Haynesville, and Marcellus shale*, *46th US Rock Mechanics/Geomechanics Symposium*. Chicago: American Rock Mechanics Association.

Mavko, G., Mukerji, T., & Dvorkin, J. (2009). *The rock physics handbook: Tools for seismic analysis of porous media*. Cambridge, UK: Cambridge University Press.

Meredith, P. G. (2013). Strength recovery and vein growth during self-sealing of experimentally-induced faults in westerly granite. In *AGU Fall Meeting Abstracts*.

Mizuno, T., Ito, H., Kuwahara, Y., Imanishi, K., & Takeda, T. (2005). Spatial variation of shear-wave splitting across an active fault and its implication for stress accumulation mechanism of inland earthquakes: The Atotsugawa fault case. *Geophysical Research Letters*, *32*, L20305. https://doi.org/10.1029/2005GL023875

Ngwenya, B. T., Main, I. G., Elphick, S. C., Crawford, B. R., & Smart, B. G. (2001). A constitutive law for low-temperature creep of water-saturated sandstones. *Journal of Geophysical Research*, *106*(B10), 21,811–21,826. https://doi.org/10.1029/2001JB000403

Nishizawa, O., & Kanagawa, K. (2010). Seismic velocity anisotropy of phyllosilicate-rich rocks: Characteristics inferred from experimental and crack-model studies of biotite-rich schist. *Geophysical Journal International*, *182*(1), 375–388.

O'Connell, R. J., & Budiansky, B. (1974). Seismic velocities in dry and saturated cracked solids. *Journal of Geophysical Research*, *79*(35), 5412–5426. https://doi.org/10.1029/JB079i035p05412

Peng, S., & Podnieks, E. R. (1972). Relaxation and the behavior of failed rock. In *International Journal of Rock Mechanics and Mining Sciences & Geomechanics Abstracts* (Vol. 9, pp. 699–700). Pergamon.

Pettitt, S., Baker, C., Young, R. P., Dahlström, L. O., & Ramqvist, G. (2002). The assessment of damage around critical engineering structures using induced seismicity and ultrasonic techniques. *Pure and Applied Geophysics*, *159*(1), 179–195. https://doi.org/10.1007/PL00001250

Renard, F., Dysthe, D., Feder, J., Bjørlykke, K., & Jamtveit, B. (2001). Enhanced pressure solution creep rates induced by clay particles: Experimental evidence in salt aggregates. *Geophysical Research Letters*, *28*(7), 1295–1298. https://doi.org/10.1029/2000GL012394

Renard, F., Gratier, J.-P., & Jamtveit, B. (2000). Kinetics of crack-sealing, intergranular pressure solution, and compaction around active faults. *Journal of Structural Geology*, *22*(10), 1395–1407. https://doi.org/10.1016/S0191-8141(00)00064-X

Ross, J. V., Bauer, S. J., & Carter, N. L. (1983). Effect of the α-β quartz transition on the creep properties of quartzite and granite. *Geophysical Research Letters*, *10*(12), 1129–1132. https://doi.org/10.1029/GL010i012p01129

Sayers, C., & Kachanov, M. (1995). Microcrack-induced elastic wave anisotropy of brittle rocks. *Journal of Geophysical Research*, *100*(B3), 4149–4156. https://doi.org/10.1029/94JB03134

Schmitt, L. (1994). Etude du soutenement hydraulique des puits petroliers dans les argilites par l'essai triaxial a confinement fluide direct (Doctoral dissertation, These de doctoral INPL (ENSG de Nancy)).

Schubnel, A., Fortin, J., Burlini, L., & Gueguen, Y. (2005). Damage and recovery of calcite rocks deformed in the cataclastic regime. *Geological Society, London, Special Publications*, *245*(1), 203–221. https://doi.org/10.1144/GSL.SP.2005.245.01.10

Schubnel, A., & Guéguen, Y. (2003). Dispersion and anisotropy of elastic waves in cracked rocks. *Journal of Geophysical Research*, *108*(B2), 2101. https://doi.org/10.1029/2002JB001824

Solum, J. G., Hickman, S. H., Lockner, D. A., Moore, D. E., van der Pluijm, B. A., Schleicher, A. M., & Evans, J. P. (2006). Mineralogical characterization of protolith and fault rocks from the SAFOD main hole. *Geophysical Research Letters*, *33*, L21314. https://doi.org/10.1029/2006GL027285

Sone, H., & Zoback, M. D. (2014). Time-dependent deformation of shale gas reservoir rocks and its long-term effect on the in situ state of stress. *International Journal of Rock Mechanics and Mining Sciences*, *69*(3), 120–132. https://doi.org/10.1016/j.ijrmms.2014.04.002

Tenthorey, E., Cox, S. F., & Todd, H. F. (2003). Evolution of strength recovery and permeability during fluid–rock reaction in experimental fault zones. *Earth and Planetary Science Letters*, *206*(1–2), 161–172. https://doi.org/10.1016/S0012-821X(02)01082-8

Thomsen, L. (1986). Weak elastic anisotropy. *Geophysics*, *51*(10), 1954–1966. https://doi.org/10.1190/1.1442051

Valès, F., Minh, D. N., Gharbi, H., & Rejeb, A. (2004). Experimental study of the influence of the degree of saturation on physical and mechanical properties in Tournemire shale (France). *Applied Clay Science*, *26*(1–4), 197–207. https://doi.org/10.1016/j.clay.2003.12.032

Wang, X. Q., Schubnel, A., Fortin, J., David, E., Guéguen, Y., & Ge, H. K. (2012). High V_P/V_S ratio: Saturated cracks or anisotropy effects? *Geophysical Research Letters*, *39*, L11307. https://doi.org/10.1029/2012GL051742

Wang, X. Q., Schubnel, A., Fortin, J., Guéguen, Y., & Ge, H. K. (2013). Physical properties and brittle strength of thermally cracked granite under confinement. *Journal of Geophysical Research: Solid Earth*, *118*, 6099–6112. https://doi.org/10.1002/2013JB010340

Yamaguchi, A., Sakaguchi, A., Sakamoto, T., Iijima, K., Kameda, J., Kimura, G., … Goldsby, D. (2011). Progressive illitization in fault gouge caused by seismic slip propagation along a megasplay fault in the Nankai trough. *Geology*, *39*(11), 995–998. https://doi.org/10.1130/G32038.1

Zhang, X., Spiers, C. J., & Peach, C. J. (2010). Compaction creep of wet granular calcite by pressure solution at 28°C to 150°C. *Journal of Geophysical Research*, *115*, B09217. https://doi.org/10.1029/2008JB005853

Zhao, X. L. J., & Roegiers, J. C. (1995). Creep crack growth in shale. In *The 35th US Symposium on Rock Mechanics (USRMS)*. American Rock Mechanics Association.